



# A unique adsorption-diffusion-decomposition mechanism for hydrogen evolution reaction towards high-efficiency Cr, Fe-modified CoP nanorod catalyst

Hui Li <sup>a,1</sup>, Li Du <sup>a,1</sup>, Ying Zhang <sup>a</sup>, Xu Liu <sup>a</sup>, Shuang Li <sup>b,\*</sup>, Chun Cheng Yang <sup>a,\*</sup>, Qing Jiang <sup>a,\*</sup>

<sup>a</sup> Key Laboratory of Automobile Materials (Jilin University), Ministry of Education, and School of Materials Science and Engineering, Jilin University, Changchun 130022, China

<sup>b</sup> Nano and Heterogeneous Materials Center, School of Materials Science and Engineering, Nanjing University of Science and Technology, Nanjing 210094, China

## ARTICLE INFO

### Keywords:

Adsorption-diffusion-decomposition mechanism  
Density functional theory simulations  
Dual-metal doping  
Hydrogen evolution reaction  
CoP nanorod arrays

## ABSTRACT

The rational construction of high-efficiency transition metal phosphides catalysts for hydrogen evolution reaction (HER) is crucial since their sluggish kinetics of water dissociation remain severe barriers for HER performance. The theoretical calculations indicate a unique adsorption-diffusion-decomposition mechanism for H<sub>2</sub>O molecules on CoP (111) surface. Herein, Fe could decrease H<sub>2</sub>O decomposition barrier energies and increase the amount of active sites, along with Cr could accelerate H<sub>2</sub>O adsorption, diffusion and increase the conductivity of the reaction surface. Aided by this mechanism, a self-supported electrode of Cr and Fe dual-doped CoP nanorod arrays grown on nickel foam was prepared. The electrode only requires an overpotential of 27 mV at 10 mA cm<sup>-2</sup> for alkaline HER with excellent durability for 400 h. Moreover, the catalyst presents only 1.505 V at 10 mA cm<sup>-2</sup> for alkaline water electrolysis. This work provides an in-depth understanding on catalytic mechanism of CoP-based materials.

## 1. Introduction

The massive consumption of fossil fuels has raised concerns on environmental issues and energy crisis. Thus, constructing a sustainable energy framework is urgent [1]. Among renewable energy sources, hydrogen is used to develop fossil-free and high-density energy system to achieve environment-friendly water cycle processes [2]. The electrochemical splitting of water into hydrogen is an extremely attractive energy conversion system [3]. Conventionally, Pt-based materials with their optimal hydrogen adsorption free energy, are acknowledged as the robust hydrogen evolution reaction (HER) catalysts [4]. However, high cost along with scarcity seriously limit their widespread applications [5]. Hence, the construction of more efficient and economically effective non-precious alternatives is imperative [6].

To date, non-precious metal-based materials, for instance, transition metal nitrides [7], oxides [8], phosphides (TMPs) [9], chalcogenides [10], selenides [11], and alloys [12], have been extensively investigated. Among these materials, Co-based TMPs with numerous active sites and tunable structures, have gained attractive attentions [13].

However, the sluggish kinetics and unfavorable Gibbs free energy change of adsorbed hydrogen ( $\Delta G_{H^*}$ ) of pure CoP severely limit its catalytic activity and durability [14]. Typically, multiple strategies such as metal elements doping [15], construction of heterostructure [16], size reduction [17], and morphology modulation [18] have been adopted to optimize the HER performance of CoP. Among them, the element doping is an efficient and simplified strategy for boosting the electrochemical performance [19–21]. Unfortunately, although the heteroatom-doped CoP materials have been explored previously [22–24], their applications in electrocatalysis still remain challenging due to the unfavorable intrinsic electronic structures and unsatisfactory adsorption behaviors of active species. Thus, a series of related works are in the following-up.

Recently, it has been reported that HER has a complex mechanism owing to the source of proton donors in alkaline media [25]. In order to deeply explore it, a unique H<sub>2</sub>O adsorption, diffusion and decomposition mechanism has been proposed aided by the density functional theory (DFT) calculations, and the roles of the doped Fe and Cr atoms in alkaline HER have been clearly indicated in this work. In general, for dual-doped CoP catalysts [23], it is often believed that the two

\* Corresponding authors.

E-mail addresses: [lishuang@njust.edu.cn](mailto:lishuang@njust.edu.cn) (S. Li), [cyyang@jlu.edu.cn](mailto:cyyang@jlu.edu.cn) (C.C. Yang), [jiangq@jlu.edu.cn](mailto:jiangq@jlu.edu.cn) (Q. Jiang).

<sup>1</sup> These authors contributed equally.

components of catalysts play synergistic effects on optimizing the electronic structures of active sites and modulating the adsorption of intermediates to promote the activity of HER. Different from previous investigations, the roles of Fe and Cr have been clarified respectively in this work. The Fe atom acts as a major role for reducing the  $\text{H}_2\text{O}$  decomposition barrier energy and increasing the amount of active sites, while the Cr atom acts as an assistant role to accelerate the adsorption and diffusion of  $\text{H}_2\text{O}$ , along with increase the conductivity of the reaction surface [24,26–28].

Aided by the above unique mechanism, a self-supported electrode of Cr, Fe-modified CoP nanorod arrays grown on nickel foam (Cr, Fe-CoP/NF) was synthesized. Compared to their single-atom doped counterparts [24,29], Cr and Fe dual-doping can accelerate the catalysis process of CoP-based catalysts. As expected, the Cr, Fe-CoP/NF electrode only requires a low overpotential of 27 mV at 10 mA cm<sup>-2</sup> for HER, along with the alkaline electrolyzer used this electrode as both cathode and anode presents a low voltage of 1.505 V at 10 mA cm<sup>-2</sup> and has exceptional durability for 450 h at 100 mA cm<sup>-2</sup>, outperforming the majority of transition metal-based catalysts. Meanwhile, such excellent performance is attributed to the nanorod arrays structure, which effectively expands the specific surface area, provides more catalytic active sites, facilitates the removal of  $\text{H}_2$  bubbles, and offers the advantage of mass transfer [30]. This work combines theoretical calculations and experiments to reveal the nature behind the excellent catalytic activities of Cr, Fe-doped CoP, which provides an in-depth understanding on rational design of dual-doped CoP materials to boost alkaline HER.

## 2. Materials design aided by DFT simulations

### 2.1. Computational method

In this work, the Vienna *ab initio* simulation package (VASP) was employed in all density functional theory (DFT) calculations [31,32]. To describe the electron exchange-correlation interaction, we utilized the generalized gradient approximation (GGA) featuring the Perdew-Burke-Ernzerhof functional [33]. The projector augmented wave method was applied for modeling the electronic-ion interaction at a plane-wave cutoff energy of 450 eV [31,34]. We employed the DFT-D3 method of Grimme to describe the van der Waals forces [35]. The structure was adequately optimized under a force convergence of 0.05 eV/Å per atom with an energy accuracy of 10<sup>-5</sup> eV. The 3 × 3 × 1 and 5 × 5 × 1 *k*-point grids derived from the  $\Gamma$ -centered Monkhorst-Pack scheme were exploited to sample the Brillouin region for the structural optimization and electronic structural calculations [36]. Considering the significant correlation effects of the *d* orbitals of transition metals, we performed GGA+*U* calculations with *U* values of 2.6, 3.5, and 2.8 for Cr, Fe, and Co, respectively, and a typical value of *J* = 1 eV for the exchange parameter [37]. The charge transfer was estimated through Bader charge analysis method [38]. For avoiding interactions between neighboring layers, a vacuum region distance of at least 20 Å along the *z*-direction (vertical to the interface) was utilized [39].

The transition states for diffusion and decomposition were located using the climbing-image nudged elastic band (CINEB) method [40], which is designed to seek saddle points and minimum energy paths. We selected 7 images along these paths with a force convergence about 0.05 eV/Å per atom. The Gibbs free energy ( $\Delta G$ ) was calculated via  $\Delta G = \Delta E_{\text{DFT}} + \Delta ZPE - T\Delta S$ , where  $\Delta E_{\text{DFT}}$ ,  $\Delta ZPE$ , and  $T\Delta S$  denote the change toward adsorption energy calculated by DFT, zero-point energy, along with entropic contribution, separately. The adsorption energy was directly obtained from the corresponding VASP calculations, while the zero-point energy and enthalpy as well as entropy contributions were calculated through the VASPKIT code [40] at 298 K temperature.

### 2.2. Catalyst design

Previous studies have shown that the HER reaction for CoP has two

steps, starting from the Volmer step ( $\text{H}_2\text{O} + \text{e}^- \rightarrow \text{H}^* + \text{OH}^*$ ) (Fig. S1). The second step has two choices, the Heyrovsky step ( $\text{H}_2\text{O} + \text{e}^- + \text{H}^* \rightarrow \text{H}_2 + \text{OH}^*$ ) or Tafel step ( $\text{H}^* + \text{H}^* \rightarrow \text{H}_2$  (g)). Either in an acidic or alkaline medium,  $\Delta G_{\text{H}^*}$  could be used to describe the HER activity of the second step [41]. From Fig. S2, the  $\Delta G_{\text{H}^*}$  of P sites on CoP (111) surface are ranged from 0.27 eV to 0.07 eV, and Fe doping could further decrease the  $|\Delta G_{\text{H}^*}|$  value. Because  $|\Delta G_{\text{H}^*}|$  is very closed to zero,  $\text{H}_2$  is readily released from the CoP surface, leading to low barriers for the second steps. However, the calculation of  $\Delta G_{\text{H}^*}$  is not enough, and the kinetics of the water dissociation ( $\text{H}_2\text{O} \rightarrow \text{H}^* + \text{OH}^*$ ) in the Volmer step play a decisive role for alkaline HER. Thus, although  $|\Delta G_{\text{H}^*}|$  of CoP is even lower than that of Cr-CoP in our studies, its first step needs a higher barrier to dissociate the O-H bonds of  $\text{H}_2\text{O}$  molecules than that of Cr-CoP, and this is the rate-determining step (RDS), resulting in the sluggish kinetics, which will be discussed in detail later.

DFT simulations were applied to analyze the breaking process of O-H bond in  $\text{H}_2\text{O}$  on CoP surface by using the climbing-image nudged elastic band. Through DFT calculations, we found that the full P-rich (111) surface has the lowest surface energy (Table S1). The optimized P-rich (111) surface configuration of CoP is shown in Fig. S3a. In a 1 × 1 supercell of P-rich (111), there are six adsorption sites, named as Co (1–2) and P (1–4), respectively. Based on the mechanism mentioned above,  $^*\text{H}_2\text{O}$  molecules are dissociated to produce  $\text{H}^*$  and  $\text{OH}^*$  (RDS), in which  $\text{H}^*$  further evolves into  $\text{H}_2$ , and  $\text{OH}^*$  desorbs from the surfaces to recover the empty site for the next reaction. Hence,  $\text{H}^*$  and  $\text{OH}^*$  are the most important intermediates and the adsorption energies of  $E_{\text{H}}$  and  $E_{\text{OH}}$  might play a key role in HER electrocatalysis. From Table S2,  $\text{H}_2\text{O}$  molecules tend to adsorb on the Co1 sites, and  $\text{H}^*$  and  $\text{OH}^*$  on the P sites. As a result,  $\text{H}_2\text{O}$  dissociation on P-rich (111) has two reaction pathways. For Path I shown in Fig. 1a, the  $\text{H}_2\text{O}$  molecules adsorb on the Co1 sites and then dissociate to  $^*\text{OH}$  (on the Co1 sites) and  $^*\text{H}$  (final state FS), and  $^*\text{H}$  would then adsorb on P1, P2 or P4 site. The P3 site is exclusive due to the positive adsorption energy of H (0.04 eV) and higher value of  $\Delta G_{\text{H}^*}$  (−0.27 eV). As shown in Fig. S4, the possible FS of Path I is co-adsorption structures of OH and H on CoP (111) surface. Among these FSs, the FS-P2 structure (Fig. S4b) has the lowest total energy. Thus, the Path I should be  $^*\text{H}_2\text{O} (\text{Co}1) \rightarrow ^*\text{OH} (\text{Co}1) + ^*\text{H} (\text{P}2)$ , and the barrier energy calculated by CINEB is 1.16 eV. For Path II, the decomposition occurs on the P sites of CoP (111) surface,  $^*\text{H}_2\text{O} (\text{P}n) \rightarrow ^*\text{OH} (\text{P}n) + ^*\text{H} (\text{P}m)$ , (n, m = 1, 2, 4, m ≠ n). The P3 site is exclusive due to the positive adsorption energies of H (0.04 eV) and OH (0.05 eV), which would make the FS unstable. The distance between P1 and P2 sites ( $d_{\text{P}1-\text{P}2}$ ) is 2.687 Å, which is smaller than  $d_{\text{P}1-\text{P}4}$  (3.308 Å) and  $d_{\text{P}2-\text{P}4}$  (3.317 Å). The P2 site is excellent for catalytic reaction since the  $\Delta G_{\text{H}^*}$  (0.07 eV) is the smallest and the adsorption energy of  $\text{H}_2\text{O}$  (−0.19 eV) is the largest among P1, P2 and P4 sites. Therefore, we assume that the decomposition may occur between P1 and P2 sites. The decomposition barrier energies between Pn and Pm were calculated by CINEB and listed in Table S3. From Fig. S5, the path of  $\text{H}_2\text{O}$  dissociation is that the initial state (IS) is one  $\text{H}_2\text{O}$  molecular adsorbed on the P2 site, and the FS is one  $\text{OH}^*$  and one  $\text{H}^*$  adsorbed on the P2 and P1 sites, respectively, *i.e.*,  $^*\text{H}_2\text{O} (\text{P}2) \rightarrow ^*\text{OH} (\text{P}2) + ^*\text{H} (\text{P}1)$ . The results agree well with our assumption. Before the  $\text{H}_2\text{O}$  decomposition, the first step is that one  $\text{H}_2\text{O}$  molecule is trapped by CoP (111) surface. Because the absorption energy of  $\text{H}_2\text{O}$  on the Co1 site is the lowest (−0.31 eV vs. −0.19 eV on the P2 site), the  $\text{H}_2\text{O}$  molecules have a larger probability to adsorb on the Co1 sites, then diffuse to the adjacent P (P1 or P2) sites and finally decompose between P1 and P2 sites (Fig. 1a). Note that the barrier energy for the Path I is 1.14 eV on the Co1 site, while that for the Path II includes 0.20 eV for diffusion and 0.67 eV for decomposition on the P2 site (Fig. 1b). According to the investigation of the adsorption and dissociated process of  $\text{H}_2\text{O}$  molecules on the (111) planes, the barrier energy of  $\text{H}_2\text{O}$  decomposition on the P2 site is lower than that on the Co1 site, indicating that all the water decomposition reactions occur on the P2 sites.

Here, the formation energies of doping atoms are used to evaluate the tendency of Cr and Fe atoms to displace Co atoms. The most stable

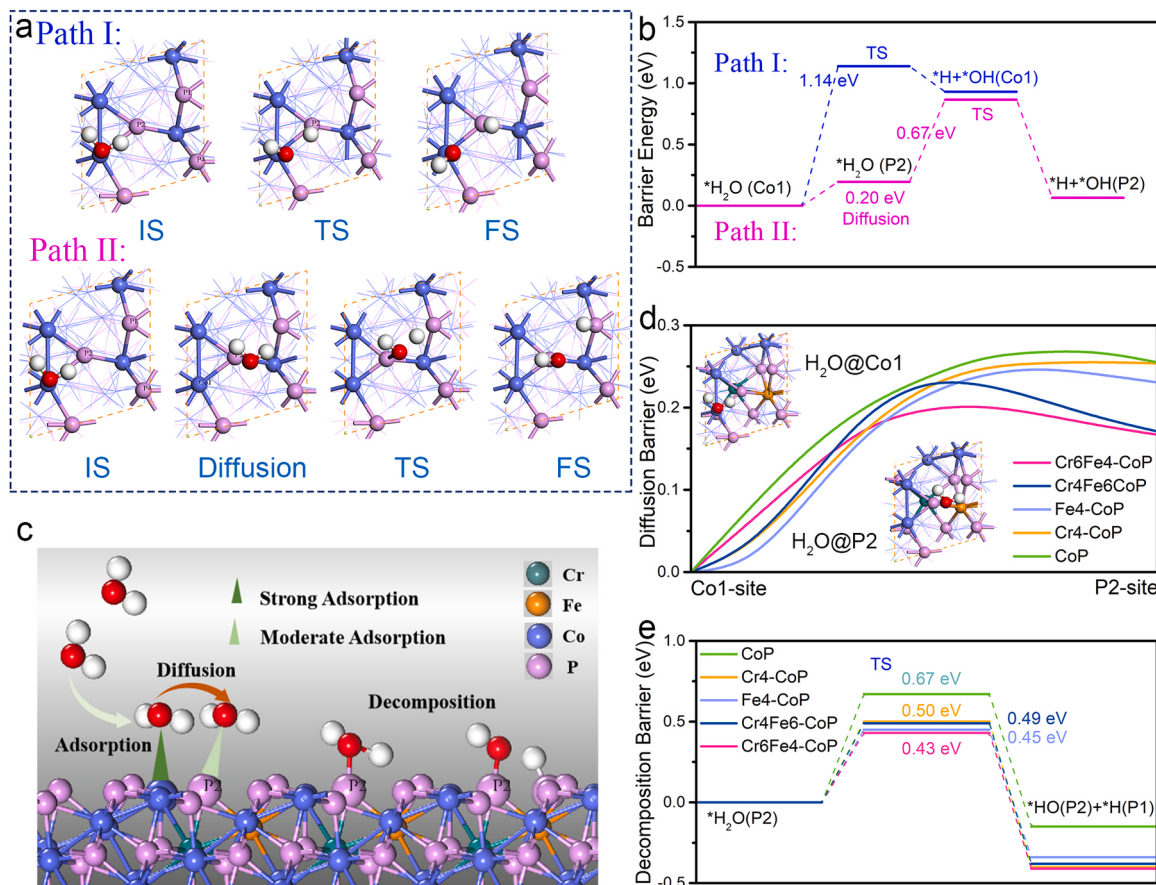


**Fig. 1.** DFT simulations. (a) Two reaction pathways for the  $\text{H}_2\text{O}$  dissociation on P-rich (111) planes. (b) Reaction barrier energies of two pathways. (c)  $\text{H}_2\text{O}$  decomposition schematic on Cr, Fe-CoP. (d) Diffusion barriers diagram and (e) decomposition barriers diagram of  $\text{H}_2\text{O}$  on CoP, Cr4-CoP, Fe4-CoP, Cr4Fe6-CoP, and Cr6Fe4-CoP.  $\text{H}_2\text{O}@\text{Co1}$  and  $\text{H}_2\text{O}@\text{P2}$  represent the  $\text{H}_2\text{O}$  molecule adsorbed on the Co1 site and adjacent P2 site, respectively.

structure of Fe-doped CoP is named as Fe4-CoP, where Fe replaces the Co4 atom at the second layer. From Table S4, Cr atom possesses a much higher formation energy than Fe atom. Therefore, Cr tends to replace the inside Co atom. The most stable dual-doped CoP is named as Cr6Fe4-CoP (Fig. S3b). For comparisons, Fe4-CoP, Cr4-CoP, Fe6-CoP, Cr6-CoP, and Cr4Fe6-CoP structures are also constructed to study the RDS barrier energies. From Fig. 1c,  $\text{H}_2\text{O}$  decomposition schematic on Cr6Fe4-CoP includes  $\text{H}_2\text{O}$  adsorption, diffusion on the surface, and then the decomposition of  $^*\text{H}_2\text{O}$  into  $^*\text{OH}$  and  $^*\text{H}$ .

The Cr (Fe)-CoP could increase  $\text{H}_2\text{O}$  adsorption and effectively decrease both  $\text{H}_2\text{O}$  diffusion (Fig. 1d) and decomposition barriers. From Fig. 1e, the RDS decomposition barriers decrease from 0.67 (CoP) to 0.43 eV (Cr6Fe4-CoP). The RDS barrier energy of Fe4-CoP is 0.45 eV, which is very close to that of Cr6Fe4-CoP (0.43 eV). When the doped sites of Fe and Cr are switched, the RDS barrier energy of Cr4Fe6-CoP increases from 0.43 to 0.49 eV, which is much close to that of Cr4-CoP (0.50 eV). Besides, the doped Cr6 (Fe6) atom has a minor effect on the  $\text{H}_2\text{O}$  decomposition (Fig. S6). Thus, for single-metal and dual-metal doped CoP, the metal atoms (Fe4 or Cr4) inject electrons into adsorbed  $^*\text{OH}$  through the Cr(Fe)-P-OH chain, where Cr and Fe atoms transform charge to the surface P atoms, resulting in the enhanced  $^*\text{OH}$  intermediate adsorption and thus optimizing the HER activity (Fig. S7). Since Cr has the smallest electronegativity value ( $\chi_{\text{Cr}} = 1.66$ ,  $\chi_{\text{Fe}} = 1.83$  and  $\chi_{\text{Co}} = 1.88$ ), it could transfer more charge to the surface P atom than Fe. Compared with the Co atom, the introduction of Cr and Fe atoms increases the average *d*-band center of the transition metal atoms, boosting the interaction of the substrate metal atoms with the surface-active P spots. Therefore, Cr (Fe) could stabilize P sites and simultaneously enhance catalytic activity during the HER process (Fig. S8).

The catalytic performance of non-metal anions active sites is mainly attributed to *p*-orbitals, and the *p*-band models play crucial effects on modulating HER. The value of  $\epsilon_p$  was calculated by using the formula

$$\epsilon_p = \int_{-\infty}^{+\infty} ED(E)dE / \int_{-\infty}^{+\infty} D(E)dE$$

where  $D(E)$  is the density of states of the *p*

band at a given energy  $E$ , and the Fermi level is assumed to be zero. To investigate the relationship between the reaction activity of Cr(Fe)-doped CoP and their orbital characteristics, we calculated the *p*-band center of the active site (P2), which is  $-1.10$  eV for pristine CoP (Fig. S9). Fe or Cr doping under P2 site makes the *p*-band center of P2 move downwards to the Fermi level. Note that the  $\Delta E$  values are not linear with the *p*-band center of the active site. Due to a larger un-filling fraction of the *p*-orbital of active site on doped-CoP, the surface P2 atom may have the stronger hybridization with the *p*-orbitals of O atom in  $^*\text{H}_2\text{O}/^*\text{OH}$ . While according to the Sabatier principle, neither too weak nor too strong binding energy between the intermediates and active sites can boost the highest catalytic activity. Thus, Cr6Fe4-CoP with *p*-band center of  $-1.13$  eV has the lowest decomposition energy barrier. The projected density of states in Fig. S8 show that the 3d-orbitals of Fe and Cr enhance its metallic nature by increasing the states close to the Fermi level. The more available states close to the Fermi level after the introduction of Cr indicate its larger contribution to the conductivity. Different from previous dual-metal doped model, in the most stable Cr6Fe4-CoP structure, the Fe atom plays a key role in reducing the  $\text{H}_2\text{O}$  decomposition barrier energies and in increasing the amount of active sites, and the Cr atom acts an assistant role in the whole reaction, which could increase the adsorption energy of  $\text{H}_2\text{O}$  on the P2 site, meanwhile accelerate the diffusion of  $\text{H}_2\text{O}$  from Co1 to P2 site (Fig. 1d). Hence, the

dual-atom doping is an effective strategy to improve the catalytic effects, which is also verified by the later experimental results. Compared with the Co atom, the introduction of Cr and Fe atoms increases the average d-band center of the transition metal atoms, boosting the interaction of the substrate metal atoms with the surface-active P spots. Therefore, Cr (Fe) could stabilize P sites and simultaneously enhance catalytic activity during the HER process.

### 3. Experimental section

#### 3.1. Materials

Nafion (5.0 wt%) and Commercial Pt/C (20%) were obtained *via* Sigma Aldrich. Cobaltous nitrate hexahydrate  $[\text{Co}(\text{NO}_3)_2 \bullet 6\text{H}_2\text{O}]$ , Ferric nitrate nonahydrate  $[\text{Fe}(\text{NO}_3)_3 \bullet 9\text{H}_2\text{O}]$ , Chromic nitrate nonahydrate  $[\text{Cr}(\text{NO}_3)_3 \bullet 9\text{H}_2\text{O}]$ , Ruthenium oxide ( $\text{RuO}_2$ ), Sodium hypophosphite monohydrate ( $\text{NaH}_2\text{PO}_2 \bullet \text{H}_2\text{O}$ ), as well as KOH were offered by Shanghai Aladdin Biochemical Technology Co. Ltd. Ar with high purity was taken from Changchun Juyang Gas Co. Ltd. Total chemical reagents obey the standards of analytical purity and can be directly usable with no further purification.

#### 3.2. Catalyst preparation

##### 3.2.1. Preparation of Cr, Fe-Co(OH)F/NF

Firstly, in order to remove surface organic molecules and oxides layers, a piece of NF was ultrasonically pre-treated with acetone and 3 M HCl aqueous solution for 20 min in turn, then rinsed using ultrapure water and ethanol, finally dried under vacuum at about 60 °C overnight. Secondly,  $\text{Co}(\text{NO}_3)_2 \bullet 6\text{H}_2\text{O}$  (1.9 mmol),  $\text{Fe}(\text{NO}_3)_3 \bullet 9\text{H}_2\text{O}$  (0.18 mmol), Cr ( $\text{NO}_3)_3 \bullet 9\text{H}_2\text{O}$  (0.1 mmol), urea (10 mmol) as well as  $\text{NH}_4\text{F}$  (5 mmol) were added to 20 ml ultrapure water, then stirred for 15 min. Next, the above acquisition was shifted to an autoclave and then maintained at 120 °C for 6 h. Finally, the attained Cr, Fe-Co(OH)F/NF was washed through ultrapure water and dried under vacuum.

##### 3.2.2. Preparation of Cr, Fe-CoP/NF

Cr, Fe-Co(OH)F/NF and 1 g  $\text{NaH}_2\text{PO}_2 \bullet \text{H}_2\text{O}$  all in small boats were situated at the downstream and upstream position of a furnace, separately. The above precursors were heated at 300 °C under Ar flow for 2 h. Afterwards, Cr, Fe-CoP/NF was obtained when the furnace cooled to room temperature. For comparisons, Fe-CoP/NF, Cr-CoP/NF, and CoP/NF were made under the similar conditions with no need to add Cr ( $\text{NO}_3)_3 \bullet 9\text{H}_2\text{O}$ ,  $\text{Fe}(\text{NO}_3)_3 \bullet 9\text{H}_2\text{O}$ , along with Cr ( $\text{NO}_3)_3 \bullet 9\text{H}_2\text{O}$  and Fe ( $\text{NO}_3)_3 \bullet 9\text{H}_2\text{O}$  in first hydrothermal procedure, separately. To optimize the doping ratio of Cr/Fe, total molar amount of the metal doping was 0.28 mmol and other two samples were made similarly *via* only adjusting the amount of  $\text{Fe}(\text{NO}_3)_3 \bullet 9\text{H}_2\text{O}$  and Cr ( $\text{NO}_3)_3 \bullet 9\text{H}_2\text{O}$ .

#### 3.3. Catalyst characterization

The nanorod arrays morphology and crystal structure for catalysts were investigated through scanning electron microscopy (SEM) (JSM-6700F, JEOL, 15 kV) and transmission electron microscopy (TEM) (JEM-2100F, JEOL, 200kV). The diffraction peaks of samples were detected under XRD technique (D/max2500pc diffractometer). XPS spectra collected the surface bonding states under a Thermo ESCALAB-250 spectrometer employing a monochromatic Al-K $\alpha$  (1253.6 eV) source. The hierarchical nanoporous structure obtained from  $\text{N}_2$  adsorption/desorption experiments was taken on a Micromeritics ASAP 2020 analyzer. The inductively coupled plasma optical emission spectrometer (ICP-OES) (Thermo Scientific) results showed the element molar ratios of cobalt-based phosphides.

#### 3.4. Electrochemical measurements

An Ivium-n-Stat electrochemical workstation was available for the electrochemical tests through the construction of a conventional three-electrode system. The cobalt-based phosphides electrode was applied for the working electrode, the  $\text{Hg}/\text{HgO}$  electrode and a graphite rod were employed as the reference electrode and the auxiliary electrode, separately. Based on the equation  $(E \text{ (vs. RHE)} = E \text{ (vs. Hg/HgO)} + 0.098 + 0.059 \times \text{pH})$ , total electrode potentials were corrected to be relative to the reversible hydrogen electrode (RHE). Moreover, ethanol (950 mL) and Nafion solution (50  $\mu\text{L}$ ) were mixed and then Pt/C (10 mg, 20 wt%) and  $\text{RuO}_2$  (10 mg) were added to the above mixture, separately, finally loaded prepared catalyst ink onto a piece of clean NF. The polarization curves with  $iR$  correction of the electrodes were obtained in Ar-saturated 1 M KOH electrolyte under 2  $\text{mV s}^{-1}$ . Electrochemical impedance spectroscopy (EIS) was applied for the 10 mV AC amplitude with an input potential of  $-0.196 \text{ V vs. RHE}$  at a frequency of 100 kHz–10 mHz. Besides, the Faradic efficiency was examined *via* a gas chromatograph [GC-2014] in the HER catalytic process.

### 4. Results and discussion

#### 4.1. Material synthesis and characterization

Based on the above DFT calculations, a self-supported Cr, Fe-CoP/NF catalyst was prepared by the classic two-step procedure from Fig. 2a. Note that the Cr/Fe ratio is 0.3:0.7 for Cr, Fe-CoP/NF in this work. At first, Cr and Fe dual-doped cobalt hydroxyl fluoride (Cr, Fe-Co(OH)F) was synthesized on NF surface by the urea hydrothermal reaction [42]. The X-ray diffraction (XRD) pattern displays signals of the precursor, which are well attributed to Ni (JCPDS 07-6667), Co ( $\text{CO}_3\text{O}_5\text{OH} \bullet 0.11\text{H}_2\text{O}$ ) (JCPDS 48-0083), as well as Co(OH)F (JCPDS 50-0827) (Fig. S10). The scanning electron microscopy (SEM) image presents the well-aligned nanorod arrays morphology of the precursor (Fig. S11a). The transmission electron microscopy (TEM) image (Fig. S11b) reveals that the nanorods exhibit the diameters of 100–200 nm with smooth surfaces.

After the phosphorization, the microstructure of Cr, Fe-CoP/NF and other comparison samples was examined by SEM. From Fig. 2b, the well-aligned nanorod arrays structure is well maintained in Cr, Fe-CoP/NF, which could provide a large surface area and facilitate the removal of  $\text{H}_2$  bubbles, thus boosting catalytic performance [43]. From Fig. S12a and b, it can be observed that the nanorods of Fe-CoP/NF are more upright relative to Cr, Fe-CoP/NF. For Cr-CoP/NF, the tips of several nanorods are cross-linked together (Fig. S12c). However, for pristine CoP/NF, some nanorods are clustered together to form the nanorod bundles structure (Fig. S12d). The above morphological changes are probably attributed to the introduction of Cr and Fe, resulting in the evolution of the nanorod arrays structure [44]. Note that the nanorod bundles are resulted from the aggregation of nanorods together, which reduces the exposed surface area. Other two samples with different Cr/Fe ratios, including  $\text{Cr}_{0.1}\text{Fe}_{0.9}\text{-CoP/NF}$  and  $\text{Cr}_{0.4}\text{Fe}_{0.6}\text{-CoP/NF}$  were also prepared through the similar synthesis strategy. Notably, the nanorods of  $\text{Cr}_{0.1}\text{Fe}_{0.9}\text{-CoP/NF}$  are still upright (Fig. S12e), while the tips of several nanorods in  $\text{Cr}_{0.4}\text{Fe}_{0.6}\text{-CoP/NF}$  are cross-linked together (Fig. S12f). The lower or higher Cr/Fe ratios can induce the morphological change of the nanorods, which further affect the number of active sites. From Fig. 2c, the TEM image reveals that the surface of the nanorod becomes rough. Remarkably, massive pores have been introduced into the nanorod after the phosphorization, which offer the advantage of mass transport in actual application [30,45]. From Fig. 2d, the high-resolution TEM (HRTEM) image exhibits that the interplanar spacings of 0.248 nm are well attributed to the (111) planes of CoP, which have the lowest surface energy based on the DFT calculations. From Fig. 2e-i, the dark field scanning TEM (STEM) and the energy-dispersive X-ray spectroscopy (EDS) images illustrate a

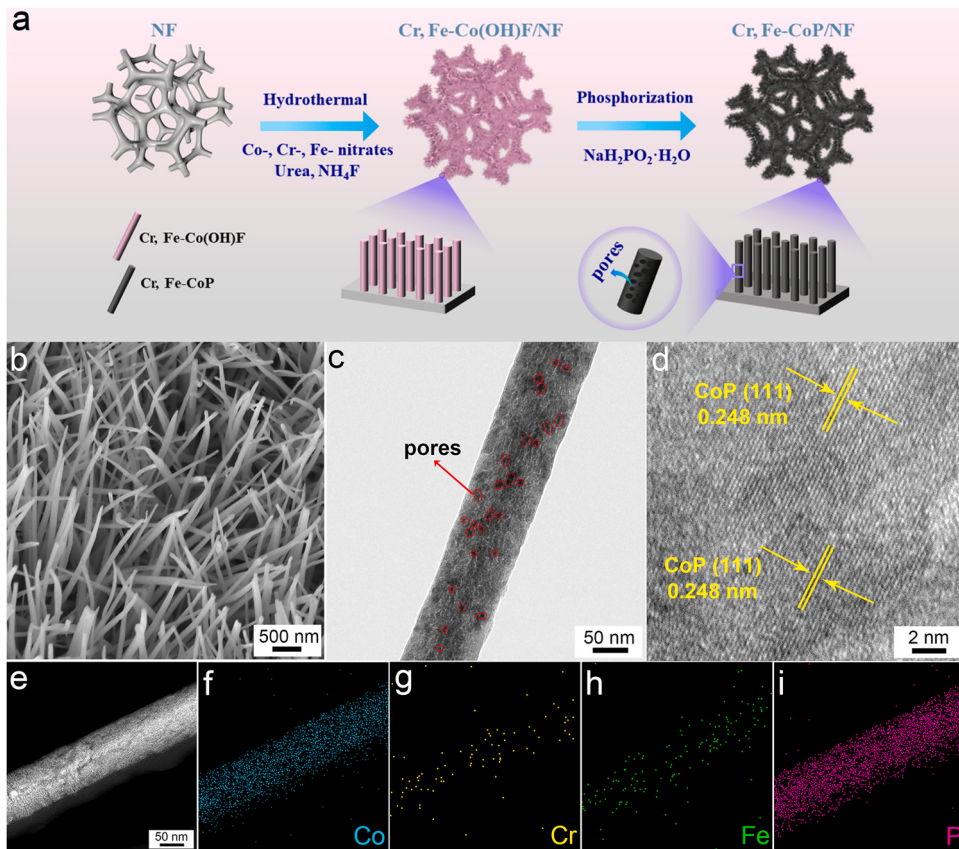


**Fig. 2.** (a) Schematic diagram about the preparation of Cr, Fe-CoP/NF. (b) SEM, (c) TEM, and (d) HRTEM images of Cr, Fe-CoP/NF. (e-i) STEM and the corresponding EDS of Co, Cr, Fe, and P in Cr, Fe-CoP/NF sample.

homogeneous distribution of Co, Fe, Cr and P on the entire nanorod, suggesting the uniform incorporation of Cr and Fe into CoP. The inductively coupled plasma optical emission spectrometer findings indicate that the element molar ratios of Co:Fe:Cr for Cr, Fe-CoP/NF, Cr<sub>0.1</sub>, Fe<sub>0.9</sub>-CoP/NF, Cr<sub>0.4</sub>, Fe<sub>0.6</sub>-CoP/NF coincide well with their feeding ratios (Table S5), indicating the universality of the synthesis method.

According to the above results, the possible synthesis principles of Cr, Fe-CoP/NF are proposed as follows. Firstly, Cr, Fe-Co(OH)F/NF was obtained through a hydrothermal method [42]. The urea was thermally decomposed into ammonium hydroxide when the hydrothermal reaction temperature reached 120 °C. During the process, Co<sup>2+</sup>, Cr<sup>3+</sup> and Fe<sup>3+</sup> co-precipitated on the NF surface, resulting in the synthesis of the Cr, Fe-Co(OH)F/NF precursor. Secondly, PH<sub>3</sub> was *in-situ* released from NaH<sub>2</sub>PO<sub>2</sub> during the thermal phosphorylation reaction (2NaH<sub>2</sub>PO<sub>2</sub>·H<sub>2</sub>O → PH<sub>3</sub> + Na<sub>2</sub>HPO<sub>4</sub> + 2 H<sub>2</sub>O) [46]. Co<sup>2+</sup> in the precursor was reduced to metallic Co via the released PH<sub>3</sub>. Meanwhile, P atoms were obtained by the oxidation and decomposition of PH<sub>3</sub> and further reacted with Co to produce CoP [47]. Note that Cr<sup>3+</sup> and Fe<sup>3+</sup> in the precursor show high reaction barriers and thus they could not be efficiently catalyzed to Cr and Fe metals. Hence, Cr and Fe were doped in CoP rather than forming the corresponding phosphides [24]. Moreover, based on the reaction-diffusion procedure dominated by the Kirkendall effect [48], Co, Cr and Fe atoms transfer to the precursor surface at various rates. At higher PH<sub>3</sub> concentrations, phosphorus diffuses into the nanorods faster than metal atoms. Therefore, the pores tend to exist in remarkably small regions, leading to the formation of porous nanorods [49]. The TEM image proves the above phenomenon. Note that the phosphorylation process was carried out at 300 °C and a small portion of the NF surface was also inevitably converted to Ni<sub>2</sub>P [50]. The corresponding XRD results confirm the above crystalline structure. From Fig. 3a, the peaks of

Cr, Fe-CoP/NF are well indexed to CoP (JCPDS 29-0497), Ni<sub>2</sub>P (JCPDS 04-5163) as well as Ni (JCPDS 07-6667). Moreover, no characteristic peaks of Cr<sub>x</sub>P and Fe<sub>x</sub>P appear, indicating the formation of Cr, Fe co-doped CoP. The comparison samples (Fe-CoP/NF, Cr-CoP/NF, as well as CoP/NF) were also detected by XRD technique (Fig. S13). Notably, with respect to CoP/NF, the CoP peaks shift toward lower angles for Fe-CoP/NF, higher angles for Cr-CoP/NF, but nearly no notable shift for Cr, Fe-CoP/NF. The slight shifts of these peaks are caused by the addition of heteroatoms with different sizes, where the ionic radii of Fe, Co, and Cr are 0.67, 0.65, and 0.62 Å, respectively. It is observed that Co possesses a smaller ionic radius than Fe and a larger than Cr, thus Cr, Fe-CoP/NF peaks show no clear shift. As reported in the literatures [15], the above results fully confirm the successful doping of Cr and Fe into Cr, Fe-CoP/NF. Through the Brunauer-Emmett-Teller results in Figs. 3b and S14, Cr, Fe-CoP/NF possesses the higher specific area (26.3 m<sup>2</sup> g<sup>-1</sup>) than CoP/NF (12.8 m<sup>2</sup> g<sup>-1</sup>). The increased surface area of Cr, Fe-CoP/NF exposes more active sites, which improve the catalytic activity. From the inset in Fig. 3b, there are the micropores (1.98 nm) and mesopores (2 ~ 10 nm) in Cr, Fe-CoP/NF through the pore size distribution diagram. Such hierarchical nanoporous structure enhances electron transfer and facilitates electrolyte penetration and gas diffusion [51].

Furthermore, the chemical compositions and electronic properties of the catalysts were probed via X-ray photoelectron spectroscopy (XPS). From the survey spectrum (Fig. S15), it can be found that Co, Fe, Cr, P, N, C, and O elements exist in Cr, Fe-CoP/NF. Notably, the O elements are caused by the inescapable superficial oxidation and adsorption of oxygen groups [52]. The presence of the C elements results from the uncontrollable carbon contamination. Besides, a few residual N elements originate from the incomplete pyrolysis in the heating process [53]. From Fig. 3c, in the Co 2p<sub>3/2</sub> region for Cr, Fe-CoP/NF, the peaks located at about 777.9 eV, 782.4 eV and 781.0 eV correspond to Co-P bond

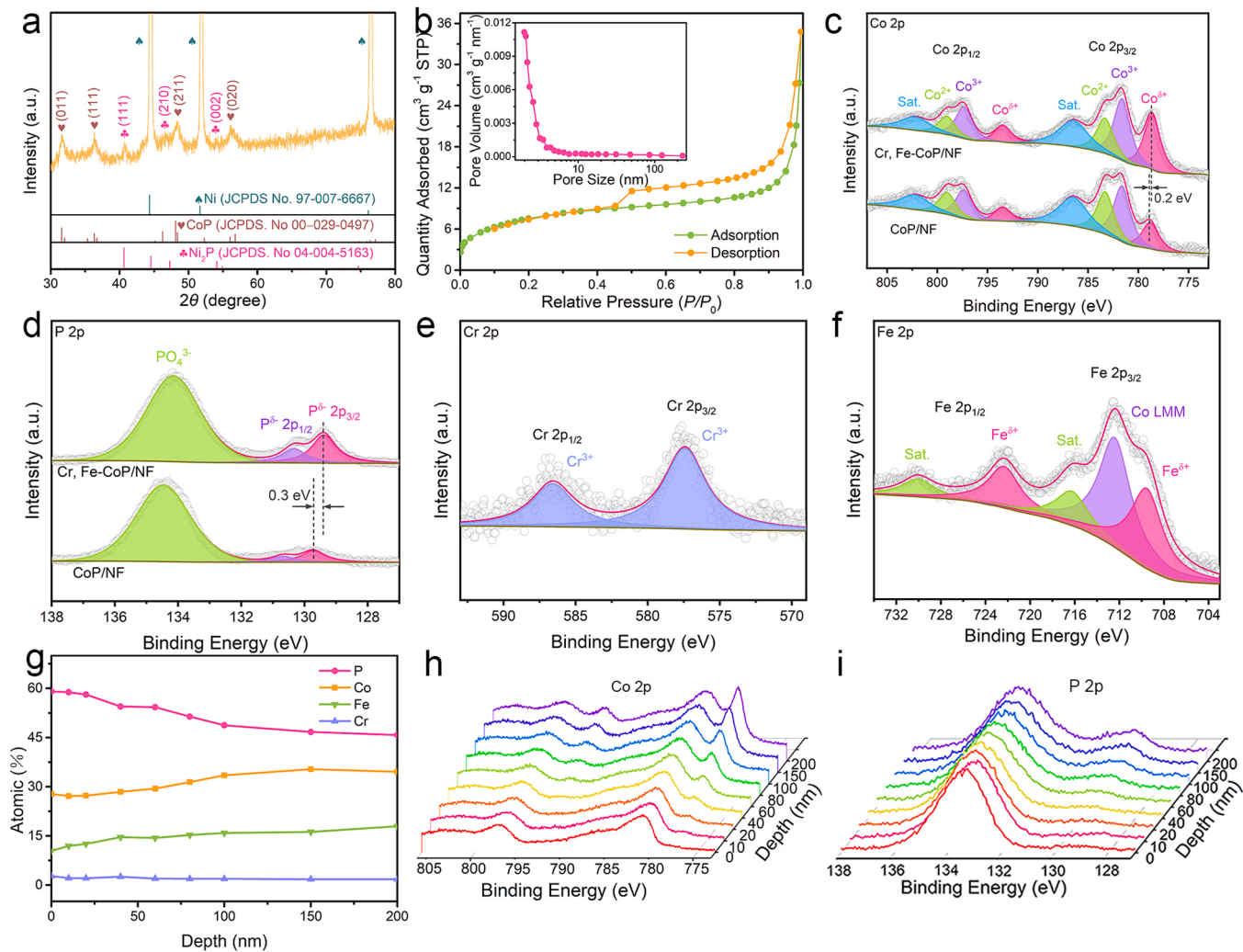


**Fig. 3.** (a) XRD pattern of Cr, Fe-CoP/NF. (b)  $N_2$  adsorption/desorption isotherms with pore size distribution (the inset) of Cr, Fe-CoP/NF. (c) Co 2p, (d) P 2p spectra for Cr, Fe-CoP/NF and CoP/NF. (e) Cr 2p, and (f) Fe 2p spectra for Cr, Fe-CoP/NF. (g) P, Co, Fe and Cr distribution ratio for Cr, Fe-CoP/NF by XPS depth. (h) Co 2p and (i) P 2p depth-profiling XPS spectra for Cr, Fe-CoP/NF.

(denoted as  $Co^{\delta+}$ ),  $Co^{2+}$  and  $Co^{3+}$ , respectively [54]. For Cr, Fe-CoP/NF, the binding energy of  $Co^{\delta+}$  peak exhibits a negative shift of 0.2 eV relative to CoP/NF. The peak centered at 128.6 eV belongs to the phosphide state (named as  $P^{\delta-}$ ), which shifts to a smaller binding energy (0.3 eV) (Fig. 3d) [55]. Combined with the DFT simulations, the Cr and Fe atoms transform charge to the surface P atoms, which enhances the \*OH intermediate adsorption and thus optimizes the HER activity. In the Cr 2p<sub>3/2</sub> region (Fig. 3e), the peak at 577.5 eV belongs to  $Cr^{3+}$  [24]. The Cr atom with low electronegativity can easily donate electrons and turn into the electron-deficient cations  $Cr^{3+}$ . High-valent Cr ( $Cr^{3+}$ ) exhibits a positive effect on the surface protection from oxidation [26]. In the Fe 2p<sub>3/2</sub> region (Fig. 3f), the peak at 709.6 eV is ascribed to  $Fe^{2+/3+}$  (denoted as  $Fe^{\delta+}$ ) and the observed broad peak centered at 712.4 eV is the Auger peak of Co [56,57]. Moreover, the depth-profiling XPS of Cr, Fe-CoP/NF investigate the specific content and chemical changes of Co, P, Cr, and Fe at different depths. From Fig. 3g, the P atoms are the most abundant and mainly distribute on the surface and subsurface. The Cr and Fe atoms partly diffuse to the subsurface or the inner core region. This is consistent with the DFT simulations, where the doped atoms replace the Co atoms at the subsurface to form the most stable structure. For Co 2p and P 2p spectra (Fig. 3h and i), the intensities of the phosphide state peaks enhance as the depth increases, which is due to the unavoidable oxidation of the surface while the inner core region is almost unaffected by oxygen. For the Cr 2p region (Fig. S16), the

characteristic peaks of different depths show little change. The intensity of the Fe characteristic peaks gradually increases with depth, indicating that Fe atoms are more distributed on the subsurface (Fig. S17).

#### 4.2. HER performance

To probe the roles of the Cr and Fe dopants for HER activities, the polarization curves (after  $iR$  correction) of our obtained samples were examined in 1 M KOH electrolyte. From Fig. 4a, the Cr, Fe-CoP/NF electrode only requires a low overpotential (27 mV) at  $10 \text{ mA cm}^{-2}$ , much smaller than Fe-CoP/NF (74 mV), Cr-CoP/NF (79 mV), CoP/NF (89 mV), and NF (285 mV), almost approaching the commercial Pt/C/NF (16 mV). Through the DFT simulations, the introduction of Cr and Fe remarkably increases  $H_2O$  adsorption and effectively decreases both  $H_2O$  diffusion and decomposition barriers. Besides, the effect of Cr/Fe ratio in  $Cr_x, Fe_y$ -CoP/NF for the electrocatalytic activity was also studied. Fig. S18 shows that Cr, Fe-CoP/NF exhibits higher alkaline HER activity (27 mV) at  $10 \text{ mA cm}^{-2}$  than  $Cr_{0.1}, Fe_{0.9}$ -CoP/NF (46 mV),  $Cr_{0.4}, Fe_{0.6}$ -CoP/NF (49 mV) and Cr, Fe-Co(OH)F (273 mV). These suggest that the appropriate Cr/Fe ratio along with the phosphorization procedure take important parts in enhancing the electrocatalytic activity. From Fig. 4b, the Tafel slope of Cr, Fe-CoP/NF is  $58 \text{ mV dec}^{-1}$ , superior to those of Fe-CoP/NF ( $67 \text{ mV dec}^{-1}$ ), Cr-CoP/NF ( $70 \text{ mV dec}^{-1}$ ), CoP/NF ( $81 \text{ mV dec}^{-1}$ ), NF ( $125 \text{ mV dec}^{-1}$ ), and only second to Pt/C/

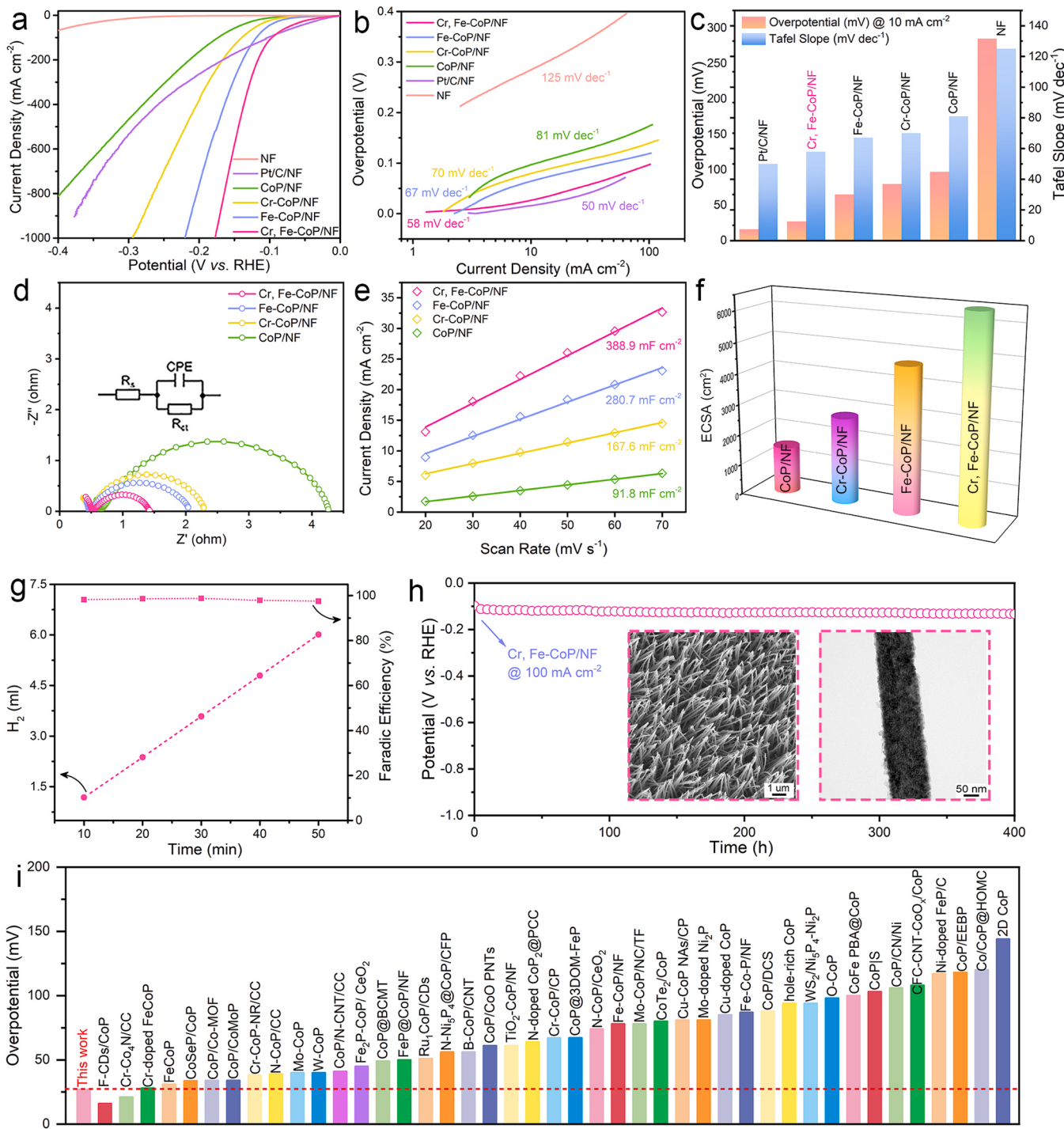


**Fig. 4.** (a) HER polarization curves for the Cr, Fe-CoP/NF, Fe-CoP/NF, Cr-CoP/NF, CoP/NF, Pt/C/NF and pure NF electrodes. (b) The corresponding Tafel plots for these electrocatalysts obtained from their polarization curves in (a). (c) Comparisons for overpotentials at 10 mA cm<sup>-2</sup> and Tafel slopes. (d) EIS plots for the Cr, Fe-CoP/NF, Fe-CoP/NF, Cr-CoP/NF, CoP/NF electrodes. The inset of (d) shows the equivalent circuit. (e) Capacitive current densities at -0.85 V (vs. Hg/HgO) plotted with various scan rates. (f) ECSA derived from  $C_{dl}$ . (g) Faradic efficiency of Cr, Fe-CoP/NF for H<sub>2</sub> evolution. (h) Chronopotentiometric test for Cr, Fe-CoP/NF at 100 mA cm<sup>-2</sup>. The insets of (h) are SEM and TEM photos of Cr, Fe-CoP/NF after HER durability test. (i) Comparisons for overpotentials at 10 mA cm<sup>-2</sup> of Cr, Fe-CoP/NF with non-precious metal alkaline HER catalysts materials in 1 M KOH (Table S6 for more details).

NF (50 mV dec<sup>-1</sup>). Such superior catalytic activities of Cr, Fe-CoP/NF are shown in Fig. 4c. The above fast HER kinetics of Cr, Fe-CoP/NF could be verified through electrochemical impedance spectroscopy (EIS) tests. From Fig. 4d, the Cr, Fe-CoP/NF electrode shows the smallest charge transfer resistance ( $R_{ct}$ ) ( $\approx 0.9 \Omega$ ) with respect to Fe-CoP/NF ( $\approx 1.5 \Omega$ ), Cr-CoP/NF ( $\approx 1.8 \Omega$ ), and CoP/NF ( $\approx 3.6 \Omega$ ), confirming the substantially boosted electrical conductivity of Cr, Fe-CoP/NF. Note that

the  $R_{ct}$  of Cr-CoP/NF is nearly  $\sim 1$  times lower than that of CoP/NF, implying that Cr doping could further increase the conductivity of the electrode and thus improve the performance of Cr, Fe-CoP/NF. Moreover, the electrochemical double-layer capacitance ( $C_{dl}$ ) was analyzed from the cyclic voltammetry (CV) curves at diverse scan rates (Fig. S19). Fig. 4e shows that Cr, Fe-CoP/NF possesses the highest  $C_{dl}$  (388.9 mF cm<sup>-2</sup>), nearly  $\sim 0.4$ ,  $\sim 1.3$  and  $\sim 3.2$  times higher than Fe-CoP/NF (280.7

$\text{mF cm}^{-2}$ ), Cr-CoP/NF (167.6  $\text{mF cm}^{-2}$ ), and CoP/NF (91.8  $\text{mF cm}^{-2}$ ), respectively. The increased electrochemical active surface area (ECSA) calculated via  $C_{\text{dl}}$  may be the origin of the enhanced geometric current density of Cr, Fe-CoP/NF (Fig. 4f) [53]. Meanwhile, for the single atom doped CoP, Fe-CoP/NF has a higher  $C_{\text{dl}}$  value than that of Cr-CoP/NF, which indicates that Fe doping could bring larger ECSA and thus provide more active sites. To investigate the relationship between Cr/Fe ratios and the number of active sites, the  $C_{\text{dl}}$  values of  $\text{Cr}_{0.1}$ ,  $\text{Fe}_{0.9}$ -CoP/NF and  $\text{Cr}_{0.4}$ ,  $\text{Fe}_{0.6}$ -CoP/NF are also obtained by performing CV tests (Fig. S20a and b). From Fig. S20c, Cr, Fe-CoP/NF exhibits the highest  $C_{\text{dl}}$  (388.9  $\text{mF cm}^{-2}$ ) compared with  $\text{Cr}_{0.1}$ ,  $\text{Fe}_{0.9}$ -CoP/NF (308.4  $\text{mF cm}^{-2}$ ) and  $\text{Cr}_{0.4}$ ,  $\text{Fe}_{0.6}$ -CoP/NF (293.3  $\text{mF cm}^{-2}$ ). This indicates that the sample with an appropriate Cr/Fe ratio exhibits significantly larger ECSA, further suggesting the increased amount of active sites. Moreover, the specific activity was gained from the polarization curves normalized by ECSA. From Fig. S21, Cr, Fe-CoP/NF owns the highest specific activity of  $17.4 \mu\text{A cm}^{-2}_{\text{ECSA}}$  at 0.1 V, which is nearly  $\sim 0.8$ ,  $\sim 1.1$ , and  $\sim 1.7$  times higher than those of Fe-CoP/NF (9.89  $\mu\text{A cm}^{-2}_{\text{ECSA}}$ ), Cr-CoP/NF (8.38  $\mu\text{A cm}^{-2}_{\text{ECSA}}$ ), and CoP/NF (6.5  $\mu\text{A cm}^{-2}_{\text{ECSA}}$ ). From Fig. S22, Cr, Fe-CoP/NF owns the higher turnover frequency (TOF) value ( $0.054 \text{ s}^{-1}$  @ 0.1 V) than Fe-CoP/NF ( $0.031 \text{ s}^{-1}$ ), Cr-CoP/NF ( $0.025 \text{ s}^{-1}$ ), and CoP/NF ( $0.022 \text{ s}^{-1}$ ). The above highest specific activity and the largest TOF value of Cr, Fe-CoP/NF indicate its remarkable intrinsic activity, thus contributing to its superior HER activity [30]. From Fig. 4g, the Faradic efficiency of Cr, Fe-CoP/NF achieves 98.2% and the realistic rate of  $\text{H}_2$  output reaches  $3.59 \text{ ml min}^{-1}$ , reflecting the few side reactions in the catalytic process. Considering massive  $\text{H}_2$  bubbles generated from cathode at high current densities ( $> 50 \text{ mA cm}^{-2}$ ), we conducted a multi-step chronopotentiometric test in 1 M KOH to assess the mass transport of Cr, Fe-CoP/NF (Fig. S23) [58]. During the HER process, the generation and release of bubbles affect the effective surface area and the stability of the polarization curve at high current densities [59]. Herein, the current density raises up to  $500 \text{ mA cm}^{-2}$  with 11 steps and decreases back to  $50 \text{ mA cm}^{-2}$  again in the same steps. According to the potential changes, the potential initially flattens quickly at  $-0.114 \text{ V}$  vs. RHE and then maintains nearly stable for the remaining 600 s. Also, the similar behaviors exhibit at other current densities. The above results reflect that the catalyst could facilitate the outward release of  $\text{H}_2$  bubbles and the inward release of OH with fast mass transport property, greatly reducing the fluctuations of the curves [58].

Besides, the chronopotentiometry test was performed at  $100 \text{ mA cm}^{-2}$  in 1 M KOH electrolyte. From Fig. 4h, the overpotential for the Cr, Fe-CoP/NF electrode shows no evident attenuation after the operation for 400 h, indicating the superior long-term HER stability. From the SEM and TEM images inserted in Fig. 4h, the retention of nanorod arrays structure indicates the outstanding structural stability. Noticeably, the remarkable HER catalytic properties of Cr, Fe-CoP/NF exceed those of most recently reported transition metal-based catalyst materials (Fig. 4i and Table S6 for details). From the XRD pattern, the catalyst after the HER durability measurement (denoted as post-HER) still maintains the initial phase structure (Fig. S24a). From Fig. S24b, the HRTEM image exhibits that the interplanar spacings of 0.248 nm are well attributed to the (111) planes of CoP. From the XPS spectra, the Cr 2p and Fe 2p spectra exhibit no obvious change relative to the initial one (Fig. S25a and b). In the Co 2p<sub>3/2</sub> region (Fig. S25c), the intensity of the peak assigned to  $\text{Co}^{\delta+}$  in the Co-P bond (777.9 eV) becomes lower after the stability testing, indicating slight oxidation of the post-HER sample. Similarly, the P 2p spectrum further confirms this trend through the attenuation of the peak intensity of  $\text{P}^{\delta-}$  (Fig. S25d). Apart from the partial oxidation of the sample surface, Cr, Fe-CoP/NF holds initial surface composition during the HER process.

#### 4.3. OER performance and overall water splitting

The OER properties for the Cr, Fe-CoP/NF pre-electrocatalyst were

examined in 1 M Ar-saturated KOH. To realize the optimized OER activity, the linear sweep voltammetry (LSV) tests of the samples with various Cr/Fe ratios were also performed. Fig. S26 shows that Cr, Fe-CoP/NF only requires an overpotential of 216 mV at  $10 \text{ mA cm}^{-2}$ , smaller than those of  $\text{Cr}_{0.1}$ ,  $\text{Fe}_{0.9}$ -CoP/NF (225 mV) and  $\text{Cr}_{0.4}$ ,  $\text{Fe}_{0.6}$ -CoP/NF (250 mV). The above results suggest that the appropriate Cr/Fe ratio has a significant impact on optimizing the OER electrocatalytic performance of  $\text{Cr}_x$ ,  $\text{Fe}_y$ -CoP/NF. From Fig. S27a, Cr, Fe-CoP/NF requires a low overpotential (216 mV @  $10 \text{ mA cm}^{-2}$ ), in clear contrast with Cr-CoP/NF (231 mV), Fe-CoP/NF (248 mV), CoP/NF (273 mV), RuO<sub>2</sub>/NF (306 mV) as well as NF (393 mV). The above results also prove the important effects of Cr and Fe dopants for Cr, Fe-CoP/NF in improving alkaline OER activity. Cr, Fe-CoP/NF possesses the lowest Tafel slope ( $38 \text{ mV dec}^{-1}$ ), in clear contrast with Fe-CoP/NF ( $42 \text{ mV dec}^{-1}$ ), Cr-CoP/NF ( $64 \text{ mV dec}^{-1}$ ), CoP/NF ( $78 \text{ mV dec}^{-1}$ ), RuO<sub>2</sub>/NF ( $93 \text{ mV dec}^{-1}$ ), as well as NF ( $111 \text{ mV dec}^{-1}$ ) (Fig. S27b). The more fast OER reactive kinetics is realized by the introduction of Cr and Fe. From Fig. S27c, the Nyquist plots illustrate the smallest charge transfer resistance for Cr, Fe-CoP/NF ( $\approx 1.4 \Omega$ ) among all the studied electrodes, implying the exceptional charge-transfer kinetics for Cr, Fe-CoP/NF during the OER catalysis. Moreover, to evaluate the potential of Cr, Fe-CoP/NF for practical applications, its Faraday efficiency and actual oxygen production were tested. As shown in Fig. S27d, the Faradic efficiency of Cr, Fe-CoP/NF is up to 98.1% and the detected  $\text{O}_2$  evolution rate is  $2.75 \text{ ml min}^{-1}$ , implying the exceptional electrochemical efficiency of Cr, Fe-CoP/NF in generating high-purity  $\text{O}_2$ . The amount of generated  $\text{O}_2$  is essentially the same as the theoretical yield, further demonstrating the excellent OER performance of Cr, Fe-CoP/NF. Cr, Fe-CoP/NF also exhibits exceptional OER durability at  $100 \text{ mA cm}^{-2}$  for 450 h (Fig. S28). After the stability test, the SEM and TEM images of the Cr, Fe-CoP/NF electrode (denoted as post-OER) display the well-retained nanorod arrays morphology, illustrating the structure stability of the catalyst (Fig. S29a and b). From the HRTEM image (Fig. S29c), the lattice spacings of 0.247 and 0.214 nm are well matched to the (111) and (200) planes of CoP and CoOOH, respectively. The corresponding SAED pattern also shows the (111) lattice plane of CoP, as well as the (200) and (151) lattice planes of CoOOH (Fig. S29d). These results prove the formation of CoOOH, which serves as the actual OER active site, as previously reported in the literatures [60,61]. Moreover, from the Co 2p<sub>3/2</sub> region (Fig. S30a), the intensity of  $\text{Co}^{3+}$  peak at about 780.5 eV is significantly enhanced, while the peak corresponding to the Co-P bond disappears. The similar phenomenon occurs in the P 2p spectrum (Fig. S30b). These results further confirm that a thin layer of metal oxyhydroxide was formed on the post-OER sample surface. From the Cr 2p and Fe 2p spectra (Fig. S30c and d), it can be seen that the surface composition of Cr and Fe elements in the post-OER sample has no significant change relative to the initial one.

To eliminate the influence of Ni<sub>2</sub>P on HER and OER properties, a comparison sample of Cr and Fe dual-doped CoP grown on carbon paper (Cr, Fe-CoP/CP) was prepared and its electrocatalytic performance was measured. From Fig. S31a and b, the Cr, Fe-CoP/CP electrode shows overpotentials of 40 and 251 mV at  $10 \text{ mA cm}^{-2}$  for HER and OER, respectively, larger than those of the Cr, Fe-CoP/NF electrode (27 mV for HER and 216 mV for OER). The possible reason is that the conductivity of NF ( $1.46 \times 10^7 \text{ S}\cdot\text{m}^{-1}$ ) is much higher than that of CP ( $1.78 \times 10^4 \text{ S}\cdot\text{m}^{-1}$ ) [62], resulting in faster electron and ion transport and thus better catalytic properties. Besides, the HER and OER performance of pure CP substrate were also tested. From Fig. S31c and d, the NF electrode exhibits overpotentials of 285 and 393 mV at  $10 \text{ mA cm}^{-2}$  for HER and OER, respectively, much superior to those of the CP electrode (505 and 641 mV for HER and OER, respectively). Therefore, the substrate is the main cause for performance degradation. This also indicates the negligible effect of Ni<sub>2</sub>P on HER and OER activity [63–65].

Moreover, the Cr, Fe-CoP/NF electrodes were applied for the cathode and anode of water electrolysis. From Fig. 5a, the Cr, Fe-CoP/NF-based electrolyzer only requires a lower voltage of  $1.505 \text{ V}$  at  $10 \text{ mA cm}^{-2}$ , in

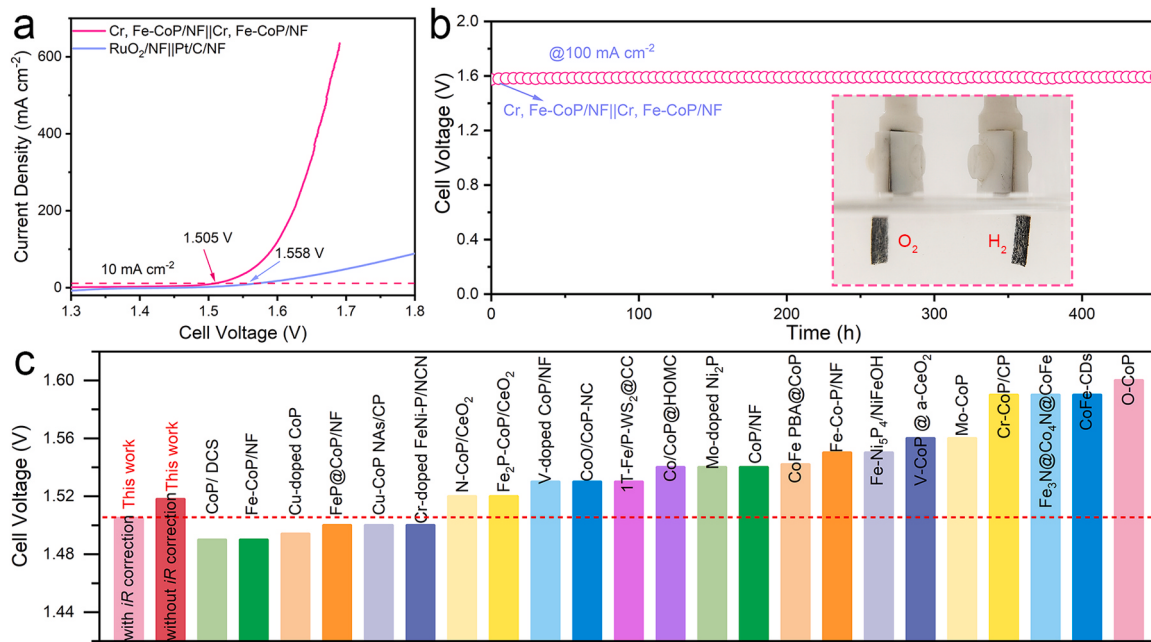


**Fig. 5.** (a) LSV curves of the Cr, Fe-CoP/NF||Cr, Fe-CoP/NF electrolyzer and the Pt/C/NF||RuO<sub>2</sub>/NF electrolyzer in 1 M KOH. (b) Chronopotentiometric test toward water electrolysis of the Cr, Fe-CoP/NF-based electrode couple at 10 mA cm<sup>-2</sup>. The photo inserted in (b) of the Cr, Fe-CoP/NF electrodes during the water electrolysis procedure. (c) Comparisons for the working voltage at 10 mA cm<sup>-2</sup> of Cr, Fe-CoP/NF with reported non-noble metal catalysts materials (Table S7 for more details).

contrast with the RuO<sub>2</sub>||Pt/C couple (1.558 V) (with *iR* correction [66–68]). The continuous generation of gas bubbles was clearly visible at both cathode and anode (the inset of Fig. 5a). It is noted that even if the curves are not corrected by *iR* (Fig. S32), the Cr, Fe-CoP/NF electrode couple exhibits a lower voltage (1.518 V) than the RuO<sub>2</sub>||Pt/C couple (1.574 V) at 10 mA cm<sup>-2</sup>. Such performance still remains a high level among the previously reported TMP-based electrocatalysts for water splitting. Furthermore, Fig. 5b shows that the Cr, Fe-CoP/NF-based electrolyzer also maintains exceptional durability at 100 mA cm<sup>-2</sup> for 450 h. Note that the cell voltage displays negligible degradation. As shown in Fig. 5c and Table S7, the outstanding water splitting performance for the Cr, Fe-CoP/NF electrode couple is superior to most of previously reported TMP-based electrocatalysts. Overall, these excellent electrochemical properties of Cr, Fe-CoP/NF imply great potential for industrial hydrogen production via alkaline water splitting.

## 5. Conclusions

In summary, aided by the DFT simulations, a self-supported Cr, Fe-CoP/NF electrode was designed and fabricated through hydrothermal and low-temperature phosphorization procedures. In the unique adsorption-diffusion-decomposition mechanism, the doped Fe atoms enhance the \*OH adsorption to decrease  $\Delta E$  and increase the amount of active sites, while the co-doped Cr atoms enhance the H<sub>2</sub>O adsorption and diffusion, along with increase the conductivity of the reaction surface, thus greatly enhancing the HER electrochemical activity. Furthermore, the porous nanorod arrays structure facilitates the mass transport and the NF substrate with high conductivity facilitates electron transfer. Hence, the catalyst shows superior HER and OER activities with  $\eta_{10}$  of 27 mV and 216 mV, separately. Furthermore, the Cr, Fe-CoP/NF-based electrolyzer only takes a working voltage of 1.505 V at 10 mA cm<sup>-2</sup> as well as exhibits exceptional durability at 100 mA cm<sup>-2</sup> for 450 h. The introduction of two foreign dopants into TMPs broadens our horizons, which is a novel strategy to design more efficient electrocatalysts for practical applications.

## CRediT authorship contribution statement

**Qing Jiang:** Writing – review & editing, Validation, Supervision, Software, Resources, Methodology, Investigation, Funding acquisition, Formal analysis, Conceptualization. **Chun Cheng Yang:** Writing – review & editing, Writing – original draft, Validation, Supervision, Resources, Project administration, Methodology, Investigation, Funding acquisition, Formal analysis, Data curation, Conceptualization. **Ying Zhang:** Investigation, Formal analysis. **Shuang Li:** Writing – review & editing, Writing – original draft, Validation, Methodology, Investigation, Formal analysis. **Xu Liu:** Investigation, Formal analysis. **Li Du:** Writing – review & editing, Writing – original draft, Validation, Methodology, Investigation, Formal analysis, Data curation. **Hui Li:** Writing – review & editing, Writing – original draft, Validation, Methodology, Investigation, Formal analysis, Data curation.

## Declaration of Competing Interest

The authors declare that they have no known competing financial interests or personal relationships that could have appeared to influence the work reported in this paper.

## Data availability

Data will be made available on request.

## Acknowledgments

H.L. and L. D. contributed equally to this work. We wish to thank the financial supports from Science and Technology Development Program of Jilin Province (No. 20230402058GH), National Natural Science Foundation of China (No. 52130101), and Graduate Innovation Funds of Jilin University (Nos. 2023CX073 and 2023CX282).

## Appendix A. Supporting information

Supplementary data associated with this article can be found in the online version at doi:10.1016/j.apcatb.2024.123749.

## References

- [1] K. Wang, H.F. Du, S. He, L. Liu, K. Yang, J.M. Sun, Y.H. Liu, Z.Z. Du, L.H. Xie, W. Ai, W. Huang, Kinetically controlled, scalable synthesis of  $\gamma$ -FeOOH nanosheet arrays on nickel foam toward efficient oxygen evolution: the key role of in-situ-generated  $\gamma$ -NiOOH, *Adv. Mater.* 33 (2021) 2005587, <https://doi.org/10.1002/adma.202005587>.
- [2] W.W. Zhong, B.B. Xiao, Z.P. Lin, Z.P. Wang, L.G. Huang, S.J. Shen, Q.H. Zhang, L. Gu, RhSe<sub>2</sub>: a superior 3D electrocatalyst with multiple active facets for hydrogen evolution reaction in both acid and alkaline solutions, *Adv. Mater.* 33 (2021) 2007894, <https://doi.org/10.1002/adma.202007894>.
- [3] H.M. Sun, C.Y. Tian, G.L. Fan, J.N. Qi, Z.T. Liu, Z.H. Yan, F.Y. Cheng, J. Chen, C. P. Li, M. Du, Boosting activity on Co<sub>4</sub>N porous nanosheet by coupling CeO<sub>2</sub> for efficient electrochemical overall water splitting at high current densities, *Adv. Funct. Mater.* 30 (2020) 1910596, <https://doi.org/10.1002/adfm.201910596>.
- [4] K.L. Zhou, Z.L. Wang, C.B. Han, X.X. Ke, C.H. Wang, Y.H. Jin, Q.Q. Zhang, J.B. Liu, H. Wang, H. Yan, Platinum single-atom catalyst coupled with transition metal/metal oxide heterostructure for accelerating alkaline hydrogen evolution reaction, *Nat. Commun.* 12 (2021) 3783, <https://doi.org/10.1038/s41467-021-24079-8>.
- [5] M. Chatenet, B.G. Pollet, D.R. Dekel, F. Dionigi, J. Deseure, P. Millet, R.D. Braatz, M.Z. Bazant, M. Eikerling, I. Staffell, P. Balcombe, Y. Shao-Horn, H. Schäfer, Water electrolysis: from textbook knowledge to the latest scientific strategies and industrial developments, *Chem. Soc. Rev.* 51 (2022) 4583–4762, <https://doi.org/10.1039/d0cs01079k>.
- [6] T.Z. Wang, X.J. Cao, L.F. Jiao, Ni<sub>2</sub>P/NiMoP heterostructure as a bifunctional electrocatalyst for energy-saving hydrogen production, *eScience* 1 (2021) 69–74, <https://doi.org/10.1016/j.esci.2021.09.002>.
- [7] Y.P. Zhang, F. Gao, D.Q. Wang, Z.L. Li, X.M. Wang, C.Q. Wang, K.W. Zhang, Y. K. Du, Amorphous/crystalline heterostructure transition-metal-based catalysts for high-performance water splitting, *Coord. Chem. Rev.* 475 (2023) 214916, <https://doi.org/10.1016/j.ccr.2022.214916>.
- [8] F. Hu, D.S. Yu, M. Ye, H. Wang, Y.A. Hao, L.Q. Wang, L.L. Li, X.P. Han, S.J. Peng, Lattice-matching formed mesoporous transition metal oxide heterostructures advance water splitting by active Fe-O-Cu bridges, *Adv. Energy Mater.* 12 (2022) 2200067, <https://doi.org/10.1002/aenm.202200067>.
- [9] B. Zhang, J.W. Shan, W.L. Wang, P. Tsakaras, Y.Y. Li, Oxygen vacancy and core-shell heterojunction engineering of anemone-like CoP@CoOOH bifunctional electrocatalyst for efficient overall water splitting, *Small* 18 (2022) 2106012, <https://doi.org/10.1002/smll.202106012>.
- [10] H.Y. Ge, G.D. Li, J.X. Shen, W.Q. Ma, X.G. Meng, L.Q. Xu, Co<sub>4</sub>N nanoparticles encapsulated in N-doped carbon box as trifunctional catalyst for Zn-air battery and overall water splitting, *Appl. Catal. B* 275 (2020) 119104, <https://doi.org/10.1016/j.apcatb.2020.119104>.
- [11] S. Ibraheem, G. Yasin, A. Kumar, M.A. Mushtaq, S. Ibrahim, R. Iqbal, M. Tabish, S. Ali, A. Saad, Iron-cation-coordinated cobalt-bridged-selenides nanorods for highly efficient photo/electrochemical water splitting, *Appl. Catal. B* 304 (2022) 120987, <https://doi.org/10.1016/j.apcatb.2021.120987>.
- [12] Z. Wang, J.M. Ang, B.W. Zhang, Y.F. Zhang, X.Y.D. Ma, T. Yan, J. Liu, B.Y. Che, Y. Z. Huang, X.H. Lu, FeCo/FeCoNi/N-doped carbon nanotubes grafted polyhedron-derived hybrid fibers as bifunctional oxygen electrocatalysts for durable rechargeable zinc-air battery, *Appl. Catal. B* 254 (2019) 26–36, <https://doi.org/10.1016/j.apcatb.2019.04.027>.
- [13] S.J. Shen, Z.P. Wang, Z.P. Lin, K. Song, Q.H. Zhang, F.Q. Meng, L. Gu, W.W. Zhong, Crystalline-amorphous interfaces coupling of CoSe<sub>2</sub>/CoP with optimized d-band center and boosted electrocatalytic hydrogen evolution, *Adv. Mater.* 34 (2022) 2110631, <https://doi.org/10.1002/adma.202110631>.
- [14] Y.N. Men, Y. Tan, P. Li, X.M. Cao, S.F. Jia, J.B. Wang, S.L. Chen, W. Luo, Tailoring the 3d-orbital electron filling degree of metal center to boost alkaline hydrogen evolution electrocatalysis, *Appl. Catal. B* 284 (2021) 119718, <https://doi.org/10.1016/j.apcatb.2020.119718>.
- [15] L. Yan, B. Zhang, J.L. Zhu, Y.Y. Li, P. Tsakaras, P.K. Shen, Electronic modulation of cobalt phosphide nanosheet arrays via copper doping for highly efficient neutral-pH overall water splitting, *Appl. Catal. B* 265 (2020) 118555, <https://doi.org/10.1016/j.apcatb.2019.118555>.
- [16] Y.Q. Wu, X. Tao, Y. Qing, H. Xu, F. Yang, S. Luo, C.H. Tian, M. Liu, X.H. Lu, Cr-doped FeNi-P nanoparticles encapsulated into N-doped carbon nanotube as a robust bifunctional catalyst for efficient overall water splitting, *Adv. Mater.* 31 (2019) 1900178, <https://doi.org/10.1002/adma.201900178>.
- [17] Q. Zhou, R. Sun, Y. Ren, R. Tian, J. Yang, H. Pang, K. Huang, X. Tian, L. Xu, Y. Tang, Reactive template-derived interfacial engineering of CoP/CoO heterostructured porous nanotubes towards superior electrocatalytic hydrogen evolution, *Carbon Energy* 5 (2023) 12, <https://doi.org/10.1002/cey2.273>.
- [18] S. Mehdi, Y. Liu, H. Wei, H. Wen, R. Shen, Z. Peng, H. Zhang, X. Wu, C. Wang, S. Guan, Co-based nanoparticles fabricated on Ni foams for efficient hydrogen generation from ammonia borane, *ACS Appl. Nano Mater.* 5 (2022) 5064–5074, <https://doi.org/10.1021/acsanm.2c00101>.
- [19] X. Hu, G. Luo, X. Guo, Q. Zhao, R. Wang, G. Huang, B. Jiang, C. Xu, F. Pan, Origin of the electrocatalytic oxygen evolution activity of nickel phosphides: in-situ electrochemical oxidation and Cr doping to achieve high performance, *Sci. Bull.* 66 (2021) 708–719, <https://doi.org/10.1016/j.scib.2020.11.009>.
- [20] E.J. Jiang, J.Q. Li, X.L. Li, A. Ali, G.F. Wang, S.J. Ma, P.K. Shen, J.L. Zhu, MoP-Mo<sub>2</sub>C quantum dot heterostructures uniformly hosted on a heteroatom-doped 3D porous carbon sheet network as an efficient bifunctional electrocatalyst for overall water splitting, *Chem. Eng. J.* 431 (2022) 133719, <https://doi.org/10.1016/j.cej.2021.133719>.
- [21] W.Z. Wu, Y.J. Huang, X.Q. Wang, P.K. Shen, J.L. Zhu, Composition-optimized manganese phosphide nanoparticles anchored on porous carbon network for efficiently electrocatalytic hydrogen evolution, *Chem. Eng. J.* 469 (2023) 143879, <https://doi.org/10.1016/j.cej.2023.143879>.
- [22] Y.N. Men, P. Li, F.L. Yang, G.Z. Cheng, S.L. Chen, W. Luo, Nitrogen-doped CoP as robust electrocatalyst for high-efficiency pH universal hydrogen evolution reaction, *Appl. Catal. B* 253 (2019) 21–27, <https://doi.org/10.1016/j.apcatb.2019.04.038>.
- [23] Y. Song, J. Cheng, J. Liu, Q. Ye, Y. Cheng, Modulating electronic structure of cobalt phosphide porous nanofiber by ruthenium and nickel dual doping for highly-efficiency overall water splitting at high current density, *Appl. Catal. B* 298 (2021) 120488, <https://doi.org/10.1016/j.apcatb.2021.120488>.
- [24] L.P. Zhang, J.T. Zhang, J.J. Fang, X.Y. Wang, L.K. Yin, W. Zhu, Z.B. Zhuang, Cr-doped CoP nanorod arrays as high-performance hydrogen evolution reaction catalysts at high current density, *Small* 17 (2021) 2100832, <https://doi.org/10.1002/smll.202100832>.
- [25] N. Yao, P. Li, Z.R. Zhou, Y.M. Zhao, G.Z. Cheng, S.L. Chen, W. Luo, Synergistically tuning water and hydrogen binding abilities over Co<sub>4</sub>N by Cr doping for exceptional alkaline hydrogen evolution electrocatalysis, *Adv. Energy Mater.* 9 (2019) 1902449, <https://doi.org/10.1002/aenm.201902449>.
- [26] Y.Y. Song, M.Z. Sun, S.C. Zhang, X.Y. Zhang, P. Yi, J.Z. Liu, B.L. Huang, M. H. Huang, L.X. Zhang, Alleviating the work function of vein-like Co<sub>3</sub>P by Cr doping for enhanced seawater electrolysis, *Adv. Funct. Mater.* 33 (2023) 2214081, <https://doi.org/10.1002/adfm.202214081>.
- [27] J. Shi, J. Ming, D. Wang, M. Wu, Improved corrosion resistance of a new 6% Cr steel in simulated concrete pore solution contaminated by chlorides, *Corros. Sci.* 174 (2020) 108851, <https://doi.org/10.1016/j.corsci.2020.108851>.
- [28] F. Yang, G. Xu, Y.B. Dou, B. Wang, H. Zhang, H. Wu, W. Zhou, J.R. Li, B.L. Chen, A flexible metal-organic framework with a high density of sulfonic acid sites for proton conduction, *Nat. Energy* 2 (2017) 877–883, <https://doi.org/10.1038/s41560-017-0018-7>.
- [29] C.F. Li, J.W. Zhao, L.J. Xie, J.Q. Wu, G.R. Li, Fe doping and oxygen vacancy modulated Fe-Ni<sub>3</sub>P<sub>4</sub>/NiFeOH nanosheets as bifunctional electrocatalysts for efficient overall water splitting, *Appl. Catal. B* 291 (2021) 119987, <https://doi.org/10.1016/j.apcatb.2021.119987>.
- [30] J.J. Ban, X.H. Wen, H.J. Xu, Z. Wang, X.H. Liu, G.Q. Cao, G.S. Shao, J.H. Hu, Dual evolution in defect and morphology of single-atom dispersed carbon based oxygen electrocatalyst, *Adv. Funct. Mater.* 31 (2021) 2010472, <https://doi.org/10.1002/adfm.202010472>.
- [31] G. Kresse, J. Furthmüller, Efficient iterative schemes for ab initio total-energy calculations using a plane-wave basis set, *Phys. Rev. B* 54 (1996) 11169–11186, <https://doi.org/10.1103/PhysRevB.54.11169>.
- [32] G. Kresse, J. Furthmüller, Efficiency of ab-initio total energy calculations for metals and semiconductors using a plane-wave basis set, *Comput. Mater. Sci.* 6 (1996) 15–50, [https://doi.org/10.1016/0927-0256\(96\)00008-0](https://doi.org/10.1016/0927-0256(96)00008-0).
- [33] J.P. Perdew, K. Burke, M. Ernzerhof, Generalized gradient approximation made simple, *Phys. Rev. Lett.* 77 (1996) 3865–3868, <https://doi.org/10.1103/PhysRevLett.77.3865>.
- [34] G. Kresse, D. Joubert, From ultrasoft pseudopotentials to the projector augmented-wave method, *Phys. Rev. B* 59 (1999) 1758–1775, <https://doi.org/10.1103/PhysRevB.59.1758>.
- [35] S. Grimme, J. Antony, S. Ehrlich, H. Krieg, A consistent and accurate ab initio parametrization of density functional dispersion correction (DFT-D) for the 94 elements H–Pu, *J. Chem. Phys.* 132 (2010) 154104, <https://doi.org/10.1063/1.3382344>.
- [36] H.J. Monkhorst, J.D. Pack, Special points for brillouin-zone integrations, *Phys. Rev. B* 13 (1976) 5188–5192, <https://doi.org/10.1103/PhysRevB.13.5188>.
- [37] S. Lany, H. Raebiger, A. Zunger, Magnetic interactions of Cr-Cr and Co-Co impurity pair in ZnO within a band-gap corrected density functional approach, *Phys. Rev. B* 77 (R) (2008) 241201, <https://doi.org/10.1103/PhysRevB.77.241201>.
- [38] J. Ciosowski, Molecular biology of prion diseases, *Science* 252 (1991) 1515–1522, <https://doi.org/10.1126/science.1675487>.
- [39] G. Henkelman, B.P. Uberuaga, H. Jónsson, A climbing image nudged elastic band method for finding saddle points and minimum energy paths, *J. Chem. Phys.* 113 (2000) 9901–9904, <https://doi.org/10.1063/1.1329672>.
- [40] V. Wang, N. Xu, J.C. Liu, G. Tang, W.T. Geng, VASPKIT: a user-friendly interface facilitating high-throughput computing and analysis using VASP code, *Comput. Phys. Commun.* 267 (2021) 108033, <https://doi.org/10.1016/j.cpc.2021.108033>.
- [41] H.Y. Jin, X. Liu, S.M. Chen, A. Vasilieff, L.Q. Li, Y. Jiao, L. Song, Y. Zheng, S.Z. Qiao, Heteroatom-doped transition metal electrocatalysts for hydrogen evolution reaction, *ACS Energy Lett.* 4 (2019) 805–810, <https://doi.org/10.1021/acsenergylett.9b00348>.
- [42] J.K. Nørskov, T. Bligaard, A. Logadottir, J.R. Kitchin, J.G. Chen, S. Pandelov, U. Stimming, Trends in the exchange current for hydrogen evolution, *J. Electrochem. Soc.* 152 (2005) J23, <https://doi.org/10.1149/1.1856988>.
- [43] J. Jiang, F.F. Sun, S. Zhou, W. Hu, H. Zhang, J.C. Dong, Z. Jiang, J.J. Zhao, J.F. Li, W.S. Yan, M. Wang, Network connectivity determines cortical thinning in early Parkinson's disease progression, *Nat. Commun.* 9 (2018) 12, <https://doi.org/10.1038/s41467-017-02416-0>.
- [44] Q. Chen, Y. Fu, J. Jin, W. Zang, X. Liu, X. Zhang, W. Huang, Z. Kou, J. Wang, L. Zhou, L. Mai, In-situ surface self-reconstruction in ternary transition metal dichalcogenide nanorod arrays enables efficient electrocatalytic oxygen evolution, *J. Energy Chem.* 55 (2021) 10–16, <https://doi.org/10.1016/j.jechem.2020.07.005>.
- [45] G. Huang, M. Hu, X.T. Xu, A.A. Alothman, M.S.S. Mushab, S.J. Ma, P.K. Shen, J. L. Zhu, Y. Yamauchi, Optimizing heterointerface of Co<sub>2</sub>P-Co<sub>3</sub>O<sub>4</sub> nanoparticles

within a porous carbon network for deciphering superior water splitting, *Small Struct.* 4 (2023) 2200235, <https://doi.org/10.1002/sst.202200235>.

[46] X. Fan, R. Sun, Y. Zhu, S. Zhang, L. Gou, L. Lu, D. Li, Controllable 3D porous Ni current collector coupled with surface phosphorization enhances Na storage of  $\text{Ni}_3\text{S}_2$  nanosheet arrays, *Small* 18 (2022) 2106161, <https://doi.org/10.1002/smll.202106161>.

[47] A.E. Henkes, Y. Vasquez, R.E. Schaak, Converting metals into phosphides: a general strategy for the synthesis of metal phosphide nanocrystals, *J. Am. Chem. Soc.* 129 (2007) 1896–1897, <https://doi.org/10.1021/ja068502l>.

[48] C. Meng, Z.M. Wang, L.J. Zhang, X.H. Ji, X.Y. Chen, R.B. Yu, Tuning the Mn dopant to boost the hydrogen evolution performance of CoP nanowire arrays, *Inorg. Chem.* 61 (2022) 9832–9839, <https://doi.org/10.1021/acs.inorgchem.2c01436>.

[49] J.T. Zhang, X. Liang, X.P. Wang, Z.B. Zhuang, CoP nanotubes formed by Kirkendall effect as efficient hydrogen evolution reaction electrocatalysts, *Mater. Lett.* 202 (2017) 146–149, <https://doi.org/10.1016/j.matlet.2017.04.154>.

[50] Y.K. Zhu, C.X. Lv, Z.C. Yin, J. Ren, X.F. Yang, C.L. Dong, H.W. Liu, R.S. Cai, Y. C. Huang, W. Theis, S.H. Shen, D.J. Yang, A [001]-oriented hittorf's phosphorus nanorods/polymeric carbon nitride heterostructure for boosting wide-spectrum-responsive photocatalytic hydrogen evolution from pure water, *Angew. Chem. Int. Ed.* 59 (2020) 868–873, <https://doi.org/10.1002/anie.201911503>.

[51] H.Y. Yang, P.F. Guo, R.R. Wang, Z.L. Chen, H.B. Xu, H.G. Pan, D.L. Sun, F. Fang, R. B. Wu, Sequential phase conversion-induced phosphides heteronanorod arrays for superior hydrogen evolution performance to Pt in wide pH media, *Adv. Mater.* 34 (2022) 2107548, <https://doi.org/10.1002/adma.202107548>.

[52] C.L. Rong, X.J. Shen, Y. Wang, L. Thomsen, T.W. Zhao, Y.B. Li, X.Y. Lu, R. Amal, C. Zhao, Electronic structure engineering of single-atom Ru sites via Co-N<sub>4</sub> sites for bifunctional pH-universal water splitting, *Adv. Mater.* 34 (2022) 2110103, <https://doi.org/10.1002/adma.202110103>.

[53] X.G. Wang, Y. Kolen'ko, L.F. Liu, Direct solvothermal phosphorization of nickel foam to fabricate integrated Ni<sub>2</sub>P-nanorods/Ni electrodes for efficient electrocatalytic hydrogen evolution, *Chem. Commun.* 51 (2015) 6738, <https://doi.org/10.1039/C5CC00370A>.

[54] S.F. Zai, X.Y. Gao, C.C. Yang, Q. Jiang, Ce-modified Ni(OH)<sub>2</sub> nanoflowers supported on NiSe<sub>2</sub> octahedra nanoparticles as high-efficient oxygen evolution electrocatalyst, *Adv. Energy Mater.* 11 (2021) 2101266, <https://doi.org/10.1002/aem.202101266>.

[55] C.J. Lyu, J. Cheng, K. Wu, J. Wu, N. Wang, Z. Guo, P. Hu, W.M. Lau, J. Zheng, Interfacial electronic structure modulation of CoP nanowires with FeP nanosheets for enhanced hydrogen evolution under alkaline water/seawater electrolytes, *Appl. Catal. B* 317 (2022) 121799, <https://doi.org/10.1016/j.apcatb.2022.121799>.

[56] P. He, X.Y. Yu, X.W.D. Lou, Carbon-incorporated nickel-cobalt mixed metal phosphide nanoboxes with enhanced electrocatalytic activity for oxygen evolution, *Angew. Chem. Int. Ed.* 56 (2017) 3897–3900, <https://doi.org/10.1002/anie.201612635>.

[57] L.M. Cao, Y.W. Hu, S.F. Tang, A. Iljin, J.W. Wang, Z.M. Zhang, T.B. Lu, Fe-CoP electrocatalyst derived from a bimetallic prussian blue analogue for large-current-density oxygen evolution and overall water splitting, *Adv. Sci.* 5 (2018) 1800949, <https://doi.org/10.1002/advs.201800949>.

[58] H.W. Xu, J.W. Zhu, P.Y. Wang, D. Chen, C.T. Zhang, M.J. Xiao, Q.L. Ma, H.W. Bai, R. Qin, J.J. Ma, S.C. Mu, Fe-Co-P multi-heterostructure arrays for efficient electrocatalytic water splitting, *J. Mater. Chem. A* 9 (2021) 24677–24685, <https://doi.org/10.1039/D1TA06603J>.

[59] Z.Y. Lu, W. Zhu, Y.Y. Yu, H.C. Zhang, Y.J. Li, X.M. Sun, X.W. Wang, H. Wang, J. M. Wang, J. Luo, X.D. Lei, L. Jiang, Ultrahigh hydrogen evolution performance of under-water “superaerophobic” MoS<sub>2</sub> nanostructured electrodes, *Adv. Mater.* 26 (2014) 2683, <https://doi.org/10.1002/adma.201304759>.

[60] W.Z. Wu, X.Y. Ma, Y.Z. Zhu, F.T. Hu, G. Huang, N.N. Wang, S.Y. Ning, Y.Q. Zhu, P. K. Shen, J.L. Zhu, Co<sub>2</sub>P-Fe<sub>2</sub>P heterogeneous nanoparticles: efficient hydrogen oxidation/evolution electrocatalysts and surface reconstruction in alkaline media, *Chem. Eng. J.* 478 (2023) 147425, <https://doi.org/10.1016/j.cej.2023.147425>.

[61] B.R. Wygant, K. Kawashima, C.B. Mullins, Catalyst or precatalyst? The effect of oxidation on transition metal carbide, pnictide, and chalcogenide oxygen evolution catalysts, *ACS Energy Lett.* 3 (2018) 2956–2966, <https://doi.org/10.1021/acsenergylett.8b01774>.

[62] P.H. Luo, L.L. Huang, Carbon paper as current collectors in graphene hydrogel electrodes for high-performance supercapacitors, *Nanomaterials* 10 (2020) 746, <https://doi.org/10.3390/nano10040746>.

[63] B. Zhou, M.Y. Li, Y.Y. Li, Y.B. Liu, Y.X. Lu, W. Li, Y.J. Wu, J. Huo, Y.Y. Wang, L. Tao, S.Y. Wang, Cobalt-regulation-induced dual active sites in Ni<sub>2</sub>P for hydrazine electrooxidation, *Chin. J. Catal.* 43 (2022) 1131–1138, [https://doi.org/10.1016/S1872-2067\(21\)63951-7](https://doi.org/10.1016/S1872-2067(21)63951-7).

[64] W.H. Zhang, X.B. Liu, Q.P. Yu, X.Y. Wang, H.M. Mao, J.Q. Chi, B. Li, J. Wan, L. Wang, In situ electronic redistribution of Ni<sub>2</sub>P hierarchical structure for energy-saving hydrogen production in seawater, *Chem. Eng. J.* 454 (2023) 140210, <https://doi.org/10.1016/j.cej.2022.140210>.

[65] X.J. Zhai, Q.P. Yu, J.Q. Chi, X.P. Wang, B. Li, B. Yang, Z.J. Li, J.P. Lai, L. Wang, Accelerated dehydrogenation kinetics through Ru, Fe dual-doped Ni<sub>2</sub>P as bifunctional electrocatalyst for hydrazine-assisted self-powered hydrogen generation, *Nano Energy* 105 (2023) 108008, <https://doi.org/10.1016/j.nanoen.2022.108008>.

[66] J.R. Feng, F. Lv, W.Y. Zhang, P.H. Li, K. Wang, C. Yang, B. Wang, Y. Yang, J. H. Zhou, F. Lin, G.C. Wang, S.J. Guo, Iridium-based multimetallic porous hollow nanocrystals for efficient overall-water-splitting catalysis, *Adv. Mater.* 29 (2017) 1703798, <https://doi.org/10.1002/adma.201703798>.

[67] S. Li, C. Xi, Y.Z. Jin, D.Y. Wu, J.Q. Wang, T. Liu, H.B. Wang, C.K. Dong, H. Liu, S. A. Kulnich, X.W. Du, Ir-O-V catalytic group in Ir-doped NiV(OH)<sub>2</sub> for overall water splitting, *ACS Energy Lett.* 4 (2019) 1823–1829, <https://doi.org/10.1021/acsenergylett.9b01252>.

[68] D. Kim, Y. Jeong, H. Roh, C. Lim, K. Yong, Biomimetic 2D-Ni(Fe)P/1D-WO<sub>x</sub> nanocoral reef electrocatalysts for efficient water splitting, *J. Mater. Chem. A* 9 (2021) 10909–10920, <https://doi.org/10.1039/D1TA01977E>.